Noise-Resilient Quantum Machine Learning for Stability Assessment of Power Systems

Yifan Zhou, *Member, IEEE* and Peng Zhang, *Senior Member, IEEE*

***Abstract*—Transient stability assessment (TSA) is a cornerstone for resilient operations of today's interconnected power grids. This paper is a confluence of quantum computing, data science and machine learning to potentially address the power system TSA issue. We devise a quantum TSA (QTSA) method to enable efficient data-driven transient stability prediction for bulk power systems, which is the first attempt to tackle the TSA issue with quantum computing. Our contributions are three-fold: 1) A high expressibility, low-depth quantum circuit (HELD) is designed for accurate and noise-resilient TSA; 2) A quantum natural gradient descent algorithm is developed for efficient HELD training; 3) A systematical analysis on QTSA's performance under various quantum factors is performed. QTSA underpins a foundation of quantum machine learning-enabled power grid stability analytics. It renders the intractable TSA straightforward and effortless in the Hilbert space, and therefore provides stability information for power system operations. Extensive experiments on quantum simulators and real quantum computers verify the accuracy, noise-resilience, scalability and universality of QTSA.**

***Index Terms*—Quantum machine learning, quantum neural network, power system stability, transient stability assessment.**

I. Introduction

Texas' and California's rolling outages [1], [2] in recent years signaled that our existing power infrastructures can hardly sustain the ever-expanding communities [3]. The situations are rapidly deteriorating as our power grids are increasingly integrating massive uncertain renewables, such as intermittent rooftop solar photovoltaics, as well as solar farms and offshore wind systems, and have been subject to more frequent weather events [4].

Interconnected power systems are the largest and most complicated man-made dynamical systems on this planet. Those bulk systems are highly nonlinear, exhibit multi-scale behaviors spatially and temporarily, and are increasingly stochastic and uncertain. A key technology to secure today's bulk power grids is transient stability assessment (TSA). Transient instability is a fast phenomenon typically taking only a few seconds for the bulk system to collapse after contingencies occur. TSA determines the system's ability to ride-through large disturbances (contingencies) and to reach the post-contingency steady-state [5]. It plays a significant role in various essential routines in power system planning and operation, such as "N-k" contingency screening [6], dynamic security analysis [7], and reliability evaluation [8]. The majority of the TSA methods rely on the explicit integration or implicit integration of differential equation models of the bulk power systems, which are known to be intractable to handle large power systems [9]. Frequent fluctuation due to deep integration of renewable energy resources and unknown models due to data privacy issues make classical TSA methods even more computationally expensive even if they are executed on the powerful real-time simulators. Transient energy function (TEF)-based methods can realize direct stability assessment without time-domain simulations [10]. Nevertheless, the obstacles in constructing a TEF for arbitrary power systems to capture all the instability modes restrict the application of TEF in large-scale, interconnected power systems [11], [12]. Due to aforementioned challenges, system operators in the control center hardly have sufficient time to steer the power system away from instability upon the occurrence of contingencies. For this reason, the artificial intelligence-based TSA without requiring manual interaction from human operators to assess the transient stability of the system has attracted significant attraction [6], [7], [13].

Today's power systems are undergoing an Enlightenment, where the confluence of big data, quantum computing and machine learning altogether is to drive a regime shift in the analysis and operation of our critical power infrastructures. Big data is the force behind the revolution: massive new types of intelligent electronic sensors such as synchronized phasor measurement units (PMUs), advanced metering infrastructure (AMI) meters and remote terminal units (RTUs) [14] are continuously generating gigantic volumes of data which allow for the development of data-driven power system analytics. Most recently, the successes in exploiting the potential of quantum supremacy [15], [16] shed lights on a "quantum leap" of computing capabilities. The power of quantum computing is derived from its ability to prepare and maintain complex superpositions of quantum states across many quantum degrees of freedom. While classically the number of required physical resources N grows exponentially with the system complexity n, N grows linearly with n in a quantum computer, resulting in exponential improvement over classical computing [17]. Furthermore, highly entangled states, very difficult to represent on classical computers, are easily represented on a quantum computer [18]. Therefore, power system problems, if formulated properly through programmable quantum circuits, can be executed efficiently on a quantum computer.

Inheriting the quantum speedup in tensor manipulation [19],

This work was supported in part by the US Department of Energy's Office of Electricity under Agreement No. 37533, in part by the US National Science Foundation under Grant Nos. ECCS-2018492, OIA-2040599 and OIA-2134840, and in part by Stony Brook University's Office of the Vice President for Research through a Quantum Information Science and Technology Seed Grant.

The authors are with the Department of Electrical and Computer Engineering, Stony Brook University, NY 11794, USA (e-mail: p.zhang@stonybrook.edu).

the swift growth in quantum machine learning (QML) techniques [20], [21] ignites new hopes of developing scalable and efficient data-driven power system analytics. QML is promising for data processing and model training in high-dimensional space [22], [23]. Ideally, unique quantum operators such as superposition and entanglement, which can not be efficiently represented by classical operators, enable a superior representation of complicated data relationships [24], [25]. Nevertheless, the existing noisy quantum devices are still restrictive, hindering the implementing of QML if deep quantum circuits are needed.

This paper is the first attempt to unlock the potential of QML for power system TSA. A high expressibility, low-depth quantum circuit-based transient stability assessment (QTSA) method is devised to enable effective data-driven transient stability prediction. The contributions of this work are threefold:

- We devise a high expressibility, low-depth quantum circuit (HELD) for QTSA that is feasible to pursue on near-term devices, considering the noisy-intermediate-scale quantum (NISQ) era [26], and also general enough to be directly expandable to the noise-free quantum computer. Through quantitative evaluations, we show that HELD exhibits the best expressibility in exploring the Hilbert space and in performing the TSA classification.
- We establish a quantum natural gradient descent algorithm to enable an efficient training of the HELD circuit along the steepest direction in the output space.
- We design systematical studies to comprehensively evaluate the TSA results under quantum environments regarding the accuracy, fidelity, and noise-resilience. By extensive experiments, we demonstrate the consistently high performance of QTSA for real-scale power systems on both quantum simulators and real quantum computers.

The remainder of the paper is organized as follows. Section II devises the QTSA methodology, including the overall framework, the HELD circuit design, and the training algorithm. Section III offers extensive case studies on both quantum simulators and real IBM quantum computers. Section IV concludes the paper.

II. Quantum Classifier for Power System TSA

A. Power System Transient Stability Assessment (TSA)

Power system transients are generically modelled as a set of nonlinear differential algebraic equations:

$$\begin{cases} \dot{X} = F_D(X, Y) & \text{(1a)} \\ 0 = F_A(X, Y) & \text{(1b)} \end{cases}$$

where X and Y separately denote the differential variables and algebraic variables; (1a) formulates the nonlinear dynamics of power devices, such as generators (e.g., synchronous machines, distributed energy resources), controllers (e.g., governors, exciters, inverters), power loads, etc; (1b) formulates the instantaneous power flow of the entire power grid.

TSA appraises a power system's capability of resisting large disturbance [5]. Denote $Z = (X, Y)$, and $\phi(t, Z)$ as the orbit of (1) starting from Z. An asymptotically stable equilibrium point (SEP) Z_s of (1) satisfies that: (a) Z_s is Lyapunov stable; (b) there exists an open neighborhood $\mathcal{O}$ of Z_s such that $\forall Z \in \mathcal{O}$ converges to Z_s when t approaches infinity [10]. The stability region of Z_s encloses all the states that can be attracted by Z_s within an infinite time:

$$\mathcal{A}(Z_s) = \{Z \in \mathbb{R}^n : \lim_{t\to\infty} \phi(t, Z) = Z_s\} \quad (2)$$

Stability region theory states that system stability after a large disturbance is determined by whether the post-disturbance state is within the stability region of an SEP [10]. Therefore, to formulate the data-driven TSA, the idea is to establish a direct mapping between the post-disturbance power system states and the stability results [6], [13].

B. Preliminaries of Quantum Computing

Machine learning tasks frequently involve high-dimensional computation. Quantum computing exhibits promising efficacy in manipulating high-dimensional vectors by tensor product of Hilbert spaces [19], which motivates us to exploit a quantum-assisted data-driven TSA.

In quantum computing, a quantum state is represented by a vector in a Hilbert space. A qubit is the fundamental element of a quantum system, which is described as $|\psi\rangle = \alpha_0 |0\rangle + \alpha_1 |1\rangle$. Here, $|0\rangle = \left[\begin{smallmatrix}1\\0\end{smallmatrix}\right]$ and $|1\rangle = \left[\begin{smallmatrix}0\\1\end{smallmatrix}\right]$ respectively denote the two-dimensional basis states; α_0 and α_1 are complex numbers; $|\alpha_0|^2$ and $|\alpha_1|^2$ respectively denote the probability on $|0\rangle$ and $|1\rangle$ satisfying $|\alpha_0|^2 + |\alpha_1|^2 = 1$. With n qubits, an arbitrary quantum state can be modelled as $|\psi\rangle = \sum_{i=1}^{2^n} \alpha_i |i\rangle$, where $|i\rangle$ represents the computational basis and $\sum_i |\alpha_i|^2 = 1$. The superposition and entanglement enable creating a complete 2^n-dimensional vector space and performing the corresponding manipulations with only n qubits [18].

A quantum circuit is a computational routine on quantum states [21]. As illustrated in Fig. 1(a), a quantum circuit consist of an ordered sequence of quantum gates $|\psi\rangle = A |\psi_0\rangle$ followed by the measurements. When parameterized quantum gates are involved, the circuit is named as a variational quantum circuit (VQC). As illustrated in Fig. 1(b), a VQC implements parameterized quantum operations $|\psi_p\rangle = A(p) |\psi_0\rangle$ according to a set of free parameters p, and therefore the output state $|\psi_p\rangle$ can be controlled by the VQC parameters. By optimizing p, VQCs can be trained to perform various tasks (e.g., linear equation solver [27], eigensolver [28]).

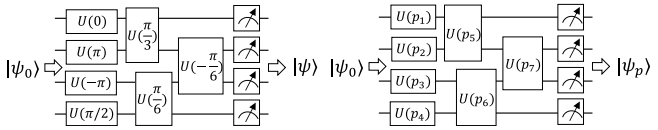

(a) Fixed quantum circuit (b) Variational quantum circuit

Fig. 1. Illustration of variational quantum circuits

Quantum machine learning (QML) takes advantages of VQCs to train a quantumized mapping between inputs and outputs. Benefiting from the aforementioned quantum speedup, QML provides an exponential improvement on computational complexity in regard of distance evaluation and inner product compared with classical computing [19].

This article has been accepted for publication in a future issue of this journal, but has not been fully edited. Content may change prior to final publication. Citation information: DOI 10.1109/TPWRS.2022.3160384, IEEE Transactions on Power Systems

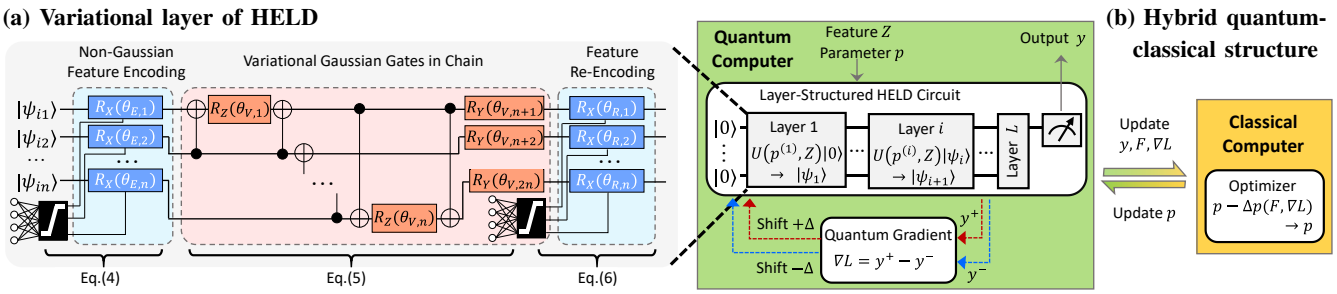

Fig. 2. **Design of high expressibility, low-depth quantum TSA. (a)**: Variational layer of HELD designed for QTSA. Each layer l consists of three blocks: a non-Gaussian feature encoding block, a variational Gaussian entangled block and a feature re-encoding block. **(b)**: Hybrid training procedure of QTSA. Quantum computer performs the feedforward execution of quantum circuits (i.e., measurement on the first qubit outputs the TSA result), and classical computer performs backward parameter update.

C. Overall Framework of QTSA

The keystone of QTSA, different from classical machine learning techniques, is that the transient stability features in a Euclidean space $Z \in \mathcal{E}$ are embedded into quantum states in a Hilbert space $|\psi\rangle \in \mathcal{H}$ through a VQC, which will explicitly separate the stable and unstable samples.

Our key innovation is a design of the *high expressibility, low-depth* circuit (HELD), as presented in Fig. 2. The *high expressibility* attribute addresses the dimensionality and nonlinearity obstacles in TSA, enabling an efficacious stability prediction for real-scale power systems. The *low-depth* attribute addresses the nonnegligible noise and source limitations in the noisy-intermediate-scale quantum era, enabling an effective execution of QTSA on near-term quantum devices. Fig. 2 depicts the variational HELD circuit, whose kernel ingredients include (see the arrangement of quantum gates in Fig. 2(a) and the corresponding mathematical formulations in section II-D):

1) Non-Gaussian feature encoding: $|\psi_E\rangle = U_E(p_E, Z)\,|0\rangle$ which adopts parameterized, activation-enhanced quantum gates to enable a flexible, nonlinear and dimension-free encoding of power system stability features Z;
2) Properly-arranged Gaussian quantum gates: $|\psi_V\rangle = U_V(p_V)\,|\psi_E\rangle$ to efficiently represent the solution space;
3) Feature re-encoding: $|\psi\rangle = U_R(p_R, Z)\,|\psi_V\rangle$ for enhanced expressibility of nonlinear behaviors in power systems;
4) Repetitive layered structure: $|\psi\rangle = U(p, Z)\,|0\rangle \triangleq U^{(L)} \cdots U^{(2)} U^{(1)}\,|0\rangle$ to realize a more expressive and entangled VQC, where $U^{(l)} = U_R^{(l)} U_V^{(l)} U_E^{(l)}$ denotes the unitary operation at l^{th} layer and p assembles the circuit parameters at each layer. The HELD circuit takes $|0\rangle$ as the input quantum state, whose state preparation is trivial.

Then, as presented in Fig. 2(b), QTSA employs a hybrid quantum-classical framework for HELD training. The parameterized HELD circuit is executed on a quantum computer as the feedforward functionality, and parameter optimization is executed on a classical computer as the backpropagation functionality. The two subroutines interact to train the VQC's parameters. Here, we introduce a generalized quantum natural gradient to enable a more efficient training of QTSA: $p - \Delta p(\nabla \mathcal{L}_y F_p^{-1} \nabla y_p) \to p$, where $\mathcal{L}$ is the nonconvex cross-entropy loss representing the correctness of quantum-embedded power system stability results; y denotes the output of the quantum circuit; ∇y_p is the quantum gradient function; $\nabla \mathcal{L}_p$ is the gradient of $\mathcal{L}$ w.r.t y; F_p is the Fisher information matrix of the non-Gaussian quantum circuit; Δp is the updating rule for circuit parameters (see details in Subsection II-E).

D. Design of HELD

Our goal is to design a powerful high expressibility, low-depth quantum circuit that processes high-dimensional inputs, embeds nonlinear power features and thus can realize stability prediction for large-scale power systems. However, the existing noisy quantum devices only allow us to execute low-depth quantum circuits. To solve this dilemma, a high expressibility, low-depth quantum circuit is established as visualized in Fig. 2. Under a multilayer structure $U = U^{(L)} \cdots U^{(2)} U^{(1)}$, each layer of HELD consists of three blocks: a non-Gaussian feature encoding block $U_E^{(l)}$, a Gaussian variational block $U_V^{(l)}$ and a feature reuploading block $U_R^{(l)}$ (see Fig. 2(a)):

$$U^{(l)}(p^{(l)}, Z) = U_R^{(l)}(p_R^{(l)}, Z) U_V^{(l)}(p_V^{(l)}) U_E^{(l)}(p_E^{(l)}, Z) \tag{3}$$

Here, $p^{(l)}$ denotes the parameters at layer l, i.e., an assembly of $p_E^{(l)}$, $p_V^{(l)}$, $p_R^{(l)}$ in each block.

The following details the mathematical representations of each block of the circuit designed in Fig. 2(a).

First, the feature encoding block (i.e., the first block in Fig. 2(a)) embeds the power system stability features a into an n-qubit quantum state. This block applies single-qubit X rotations (i.e., RX gates) at each qubit. The representation of an RX gate is $R_X(\theta) = e^{-i\theta\sigma_x/2} = \begin{bmatrix} \cos(\theta/2) & -i\sin(\theta/2) \\ -i\sin(\theta/2) & \cos(\theta/2) \end{bmatrix}$, where θ is the rotating angle and $\sigma_x = \begin{bmatrix} 0 & 1 \\ 1 & 0 \end{bmatrix}$ is the Pauli-X operator. Different rotating angles of the RX gate lead to different quantum states [21]. Therefore, by embedding the power system features into the quantum gate angles, the output states can be controlled. Consequently, the feature encoding block is realized by a unitary transform as:

$$U_E^{(l)}(p_E^{(l)}, Z) = \bigotimes_{k=1}^{n} \exp\left(-i\theta_{E,k}^{(l)} \sigma_{x,k}/2\right) \tag{4}$$

where (l) denotes the l-th layer; $p_E^{(l)}$ denotes the parameters at the l-th layer; $\bigotimes$ denotes the tensor product; $\sigma_{x,k}$ denotes the Pauli-X operator applied on the k-th qubit; $\theta_E^{(l)} = \sigma(\langle p_E^{(l)}, [Z; 1] \rangle)$ denotes the rotating angles of the

This article has been accepted for publication in a future issue of this journal, but has not been fully edited. Content may change prior to final publication. Citation information: DOI 10.1109/TPWRS.2022.3160384, IEEE Transactions on Power Systems

RX gates which adopt a single-layer perception of the input power system features to enhance the expressibility on limited quantum resources; σ is the activation function, e.g. tanh, sigmoid, ReLU.

Then, the variational block (i.e., the second block in Fig. 2(a)) is constructed to introduce entanglements between qubits, which is essential to enhance a quantum circuit's ability to express the whole Hilbert space [29]. This block is composed of two parts: a ring structure of the RZZ gates (i.e., the CNOT-RZ-CNOT gates) on each two adjacent qubits [24] and parallel single-qubit Y rotations (i.e., RY gates) on each qubit. The representations of an RZZ gate and an RY gate are respectively $R_{ZZ}(\theta) = e^{-i\theta/2\sigma_z\otimes\sigma_z}$ and $R_Y(\theta) = e^{-i\theta\sigma_y/2} = \begin{bmatrix}\cos(\theta/2) & -\sin(\theta/2)\\ \sin(\theta/2) & \cos(\theta/2)\end{bmatrix}$, where $\sigma_y = \begin{bmatrix}0 & -i\\ i & 0\end{bmatrix}$ and $\sigma_z = \begin{bmatrix}1 & 0\\ 0 & -1\end{bmatrix}$ respectively denote the Pauli-Y and Pauli-Z operators. Therefore, the mathematical representation of the variational block is as follows.

$$U_V^{(l)}(p_V^{(l)}) = \left(\prod_{k=1}^{n} I^{\otimes(k-1)} \exp\left(-i\theta_{V,k}^{(l)}\sigma_{z,k}\otimes\sigma_{z,k+1}/2\right) I^{\otimes(n-k-1)}\right) \bigotimes_{k=1}^{n} \exp\left(-i\theta_{V,k+n}^{(l)}\sigma_{y,k}/2\right) \tag{5}$$

where $\theta_V^{(l)} = p_V^{(l)}$; $\sigma_{y,k}$ and $\sigma_{z,k}$ separately denote the Pauli-Y and Pauli-Z operators on the k-th qubit. Specifically, for the 2-qubit HELD, no ring structure is required. The trainable rotations and CNOTs together generate highly entangled quantum states to capture non-trivial correlations in quantum states by a low-depth circuit, and therefore enable an efficient expression of the solution space [29].

Subsequently, feature encoding is repeated as a data-reuploading block [30] (i.e., the third block in Fig. 2(a)). The power system features are again embedded into the rotating angles of the RX gates to further enhance the expressibility for quantum stability assessment. In analogy to (4), the feature re-encoding block is formulated as:

$$U_R(p_R^{(l)}, Z) = \bigotimes_{k=1}^{n} \exp\left(-i\theta_{R,k}^{(l)}\sigma_{x,k}/2\right) \tag{6}$$

where $\theta_R^{(l)} = \sigma(\langle p_R^{(l)}, [Z;1]\rangle)$.

An arbitrary qubit of the HELD circuit can be chosen as the output qubit. A single qubit describes a two-dimensional quantum state. A mapping between stable (unstable) and higher (lower) possibility on $|1\rangle$ therefore enables the binary classification functionality of TSA. Without loss of generality, in this paper, the measurement on the first qubit, denoted as y, is selected to generate the TSA prediction result. On a quantum simulator, the expectation value of $y = \langle 0| U^\dagger(p,Z)\mathcal{M}U(p,Z)|0\rangle$ of the observable $\mathcal{M}$ is computed, where p assembles circuit parameters (i.e., $p^{(l)}$) at each layer. On a real quantum machine, the multi-shot implementation is performed to estimate y.

E. QTSA Training Through Quantum Natural Gradient

In this subsection, we establish a generalized quantum natural gradient (QNG) algorithm for efficient QTSA training. QNG is a promising algorithm for quantum optimization. It outperforms the commonly-used quantum gradient descent because of the capability of searching the steepest descent direction in the output space [31], [32]. However, existing QNG algorithms mostly resolves quadratic objective minimization of Gaussian quantum circuits [33], [34], which do not adapt to the non-Gaussian HELD training. Therefore, the following develops a generalized QNG which is able to deal with arbitrary quantum circuits and nonconvex loss functions.

Consider a training set $\{(\hat{Z}_i, \hat{y}_i)\}_{i=1}^n$, where $\hat{Z}_i$ and $\hat{y}_i$ respectively denote the TSA feature vector and the corresponding stability label of the i-th sample. The parameterized HELD circuit is optimized on the training set with a cross-entropy loss function:

$$\mathcal{L}(p) = \sum_{i=1}^{n} l(y_i(p,\hat{Z}_i)) = \sum_{i=1}^{n} -\log\Big(y_i(p,\hat{Z}_i)\Big) \tag{7}$$

Here, $y_i = \langle 0| U^\dagger(p,\hat{Z}_i)\mathcal{M}_i U(p,\hat{Z}_i)|0\rangle$ is the QTSA's prediction of the i-th sample; $\mathcal{M}_i$ is the corresponding observable, i.e., $\mathcal{M}_i = |0\rangle\langle 0|$ for $\hat{y}_i = 0$ (i.e., unstable) and $\mathcal{M}_i = |1\rangle\langle 1|$ for $\hat{y}_i = 1$ (i.e., stable).

Denoting θ as an assemble of gate rotation angles (i.e., θ_E, θ_V and θ_R), a second-order Taylor expansion of y_i w.r.t θ yields:

$$\mathrm{d}y_i \approx \frac{\partial y_i}{\partial\theta}\mathrm{d}\theta + \frac{1}{2}\mathrm{d}\theta^T f_i(\theta)\mathrm{d}\theta \tag{8}$$

Here, $\frac{\partial y_i}{\partial\theta}$ is the quantum gradient calculated by the parameter-shift rule [32]; $f_i(\theta)$ is the quantum Fisher information matrix regarding a Gaussian quantum circuit, i.e., $f_{i,jk} = \mathrm{Re}(\langle\frac{\partial\psi_i}{\partial\theta_j}, \frac{\partial\psi_i}{\partial\theta_k}\rangle - \langle\frac{\partial\psi_i}{\partial\theta_j}, \psi_i\rangle\langle\psi_i, \frac{\partial\psi_i}{\partial\theta_k}\rangle)$ and $\psi_i = U(p,\hat{Z}_i)|0\rangle$ based on the Fubini-Study metric [33].

Based on (4)-(6), substituting $\mathrm{d}\theta = \frac{\partial\theta}{\partial p}\mathrm{d}p$ into (8) yields:

$$\mathrm{d}y_i \approx \frac{\partial y_i}{\partial p}\mathrm{d}p + \frac{1}{2}\mathrm{d}p^T\left(\frac{\partial\theta}{\partial p}^T f_i(\theta)\frac{\partial\theta}{\partial p}\right)\mathrm{d}p \tag{9}$$

$F_i(p) = \frac{\partial\theta}{\partial p}^T f_i(\theta)\frac{\partial\theta}{\partial p}$ establishes the quantum Fisher matrix for a generic non-Gaussian quantum circuit. F_i represents an approximation of Hessian matrix of y_i at p and therefore enables searching the local minimal of y_i around p with second-order terms:

$$g_p^y = \arg\min_{\Delta p}[\frac{\partial y_i}{\partial p}\Delta p + \frac{1}{2}\Delta p^T F_i(p)\Delta p] = -F_i^+(p)\frac{\partial y_i}{\partial p} \tag{10}$$

where g_p^y denotes the natural gradient of y w.r.t p; F_i^+ denotes the pseudo-inverse of F_i.

Correspondingly, QNG is established for (7), where $\mathcal{L}$-optimization is iteratively solved at the steepest direction in the distribution space:

$$g_{p,k}^L = -\sum_{i\in\mathcal{B}}\frac{\partial l}{\partial y_i}F_i^+(p_k)\frac{\partial y_i}{\partial p_k} \tag{11}$$

$$p_{k+1} = p_k - \frac{\eta}{\sqrt{\hat{v}_k}+\xi}\hat{m}_k \tag{12}$$

Here, $\mathcal{B}$ denotes the batch set; k denotes the k-th iteration; η denotes the learning rate; $\hat{m}_k$ and $\hat{v}_k$ jointly realize an

This article has been accepted for publication in a future issue of this journal, but has not been fully edited. Content may change prior to final publication. Citation information: DOI 10.1109/TPWRS.2022.3160384, IEEE Transactions on Power Systems

adaptive learning rate [35], where $\hat{m}_k = m_k/(1-\beta_1^k)$, $\hat{v}_k = v_k/(1-\beta_2^k)$, $m_k = \beta_1 m_{k-1} + (1-\beta_1) g_{p,k}^L$ and $v_k = \beta_2 v_{k-1} + (1-\beta_2)(g_{p,k}^L)^2$; ξ is a small positive constant to ensure the numerical stability; β_1 and β_2 are hyperparameters governing the moment updates.

Next, we show that the non-Gaussian quantum Fisher matrix F_i can be effectively approximated in a block-diagonal form. For concision, the subscript i is omitted in the following derivation. Based on (4)-(6), we have:

$$\frac{\partial \theta}{\partial p} = \begin{array}{c} \\ \theta^{(1)} \\ \theta^{(2)} \\ \vdots \\ \theta^{(L)} \end{array} \begin{array}{c} \begin{array}{cccc} p^{(1)} & p^{(2)} & \cdots & p^{(L)} \end{array} \\ \begin{bmatrix} \nabla\theta_p^{(1)} & 0 & \cdots & 0 \\ 0 & \nabla\theta_p^{(2)} & \cdots & 0 \\ \vdots & \vdots & \ddots & \vdots \\ 0 & 0 & \cdots & \nabla\theta_p^{(L)} \end{bmatrix} \end{array} \tag{13}$$

where:

$$\nabla\theta_p^{(1)} = \begin{array}{c} \\ \theta_E^{(l)} \\ \theta_V^{(l)} \\ \theta_R^{(l)} \end{array} \begin{array}{c} \begin{array}{ccc} p_E^{(l)} & p_V^{(l)} & p_R^{(l)} \end{array} \\ \begin{bmatrix} \nabla\sigma[Z;1]^T & 0 & 0 \\ 0 & I & 0 \\ 0 & 0 & \nabla\sigma[Z;1]^T \end{bmatrix} \end{array}$$

According to [33], the Gaussian Fisher matrix f also follows a block-diagonal form. Consequently, the non-Gaussian Fisher matrix is constructed as:

$$F(p) = \begin{array}{c} \\ p^{(1)} \\ p^{(2)} \\ \vdots \\ p^{(L)} \end{array} \begin{array}{c} \begin{array}{cccc} p^{(1)} & p^{(2)} & \cdots & p^{(L)} \end{array} \\ \begin{bmatrix} F^{(1)}(p) & 0 & \cdots & 0 \\ 0 & F^{(2)}(p) & \cdots & 0 \\ \vdots & \vdots & \ddots & \vdots \\ 0 & 0 & \cdots & F^{(L)}(p) \end{bmatrix} \end{array} \tag{14}$$

Here, $F^{(l)}(p) = (\nabla\theta_p^{(l)})^T f^{(l)} \nabla\theta_p^{(l)}$; $f^{(l)}(\theta)$ denotes the Gaussian Fisher matrix block of the l^{th} layer, where $f_{jk}^{(l)} = \langle\psi^{(l)}|K_j K_k|\psi^{(l)}\rangle - \langle\psi^{(l)}|K_j|\psi^{(l)}\rangle\langle\psi^{(l)}|K_k|\psi^{(l)}\rangle$ [33]. Matrix multiplication and pseudo-inverse of a block-diagonalized $F(p)$ would be highly efficient.

Aforementioned derivations establish the generalized QNG algorithm, which adopts Riemannian metrics and enables efficient training of the HELD circuit with arbitrary gates and targets. Therefore, the optimization of HELD will be performed along the steepest descent direction in the output space, whereas the conventional quantum gradient descent is only capable of updating parameters following the steepest descent direction in the parameter space with Euclidean metrics.

III. Numerical Experiments

Extensive experiments of QTSA are conducted on typical power systems ranging from benchmark grids to a real-scale U.S. power grids. QTSA is coded with Qiskit [36] and Pennylane [37], and is implemented on both a noise-free quantum simulator (*ibmq_qasm_simulator*, a 32-qubit simulator) and real IBM quantum devices (a 20-qubit machine *ibmq_boeblingen*, and a 7-qubit machine *ibm_lagos*). Power system transient simulations with random fault locations and random fault clearing time are conducted by Power System Toolbox (PST) [38]. Those physical model-based simulations will generate the features for QTSA (such as power outputs, rotor angles and rotor speeds of generators, power flows through transmission lines, and bus voltage angles and amplitudes) as well as providing the ground truth of the system stability.

The following sections investigate the capability of QTSA in assessing power system stability on both noise-free simulators and near-term noisy quantum computers, as well as the performance of different quantum circuit designs for QTSA.

A. Validity of QTSA on Noise-Free Quantum Simulator

Four typical power systems are studied:

- *Single-machine infinite-bus (SMIB) system*, one of the most widely-used test systems in power system research. Since the stability region of SMIB (i.e., a 2-dimensional region) can be analytically computed, SMIB always serves as an indispensable benchmark for testing the performance of a TSA method.
- *Two-area system*, another most widely-used benchmark system exhibiting both local and inter-area oscillation modes. The system models and parameters are constructed from a real North American power system [5].
- *Northeast Power Coordinating Council (NPCC) test system*, a real Northeastern US power system which was involved in the Northeast blackout of 2003.
- *IEEE 300-bus system*, a large power system which contains 69 generators, 304 transmission lines, and 195 loads. Generators are formulated using the classical synchronous machine model.

Appendix A presents the test system parameters and the settings of the training and testing sets.

The overall QTSA procedure is exemplified via the SMIB system. We then verify the efficacy of QTSA on all the test systems.

1) Training Preparation: Various dynamics samples are generated on the SMIB system (see Fig. 3(a)). Time-domain simulations of SMIB under random disturbances are performed to obtain stability features (i.e., rotor angle and rotor speed in this case). Fig. 3(b) shows both the stable cases with dampened oscillations and the unstable cases where power generators run out-of-step. The initial states of the post-disturbance system therefore construct the feature set for QTSA training, as shown by the samples in Fig. 3(c) (green for stable samples and red for unstable samples). Our hope is that QTSA can directly distinguish the stable and unstable samples in the Hilbert space.

2) QTSA Training: A HELD circuit with 2 qubits, 6 layers (denoted by HELD(2,6)) is constructed for SMIB. Fig. 3(d) to (f) show how an untrained HELD evolves into a well-trained one. We use Bloch sphere and quantum states overlap to evaluate the QTSA efficacy in the Hilbert space. A point

This article has been accepted for publication in a future issue of this journal, but has not been fully edited. Content may change prior to final publication. Citation information: DOI 10.1109/TPWRS.2022.3160384, IEEE Transactions on Power Systems

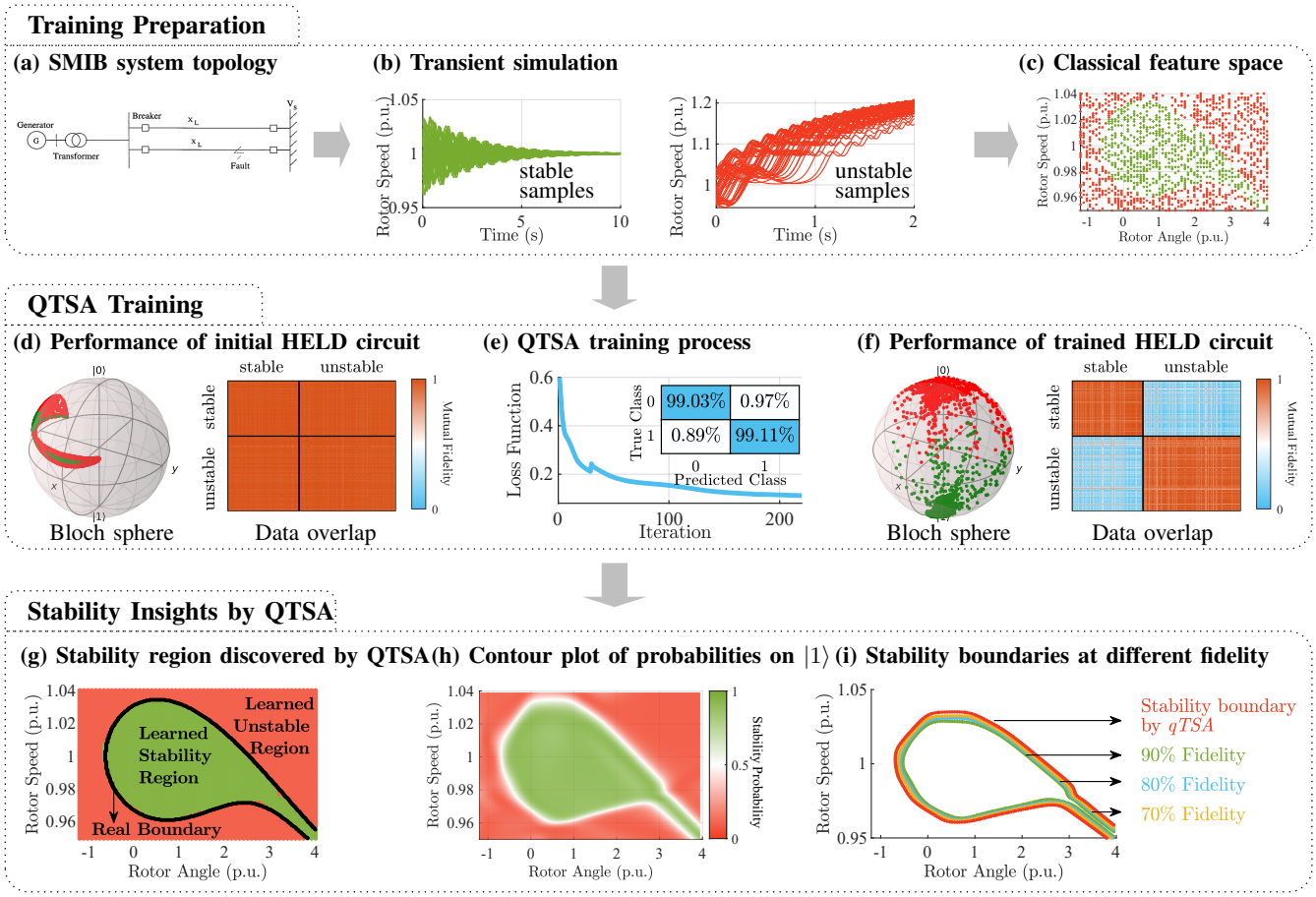

Fig. 3. **Demonstration of QTSA procedure on the SMIB test system.** Subplots (a)-(c) demonstrate training preparation. Subplots (d)-(f) demonstrate QTSA training. Subplots (g)-(i) demonstrate the stability insights obtained by QTSA learning. **(a)**: Topology of the SMIB system. **(b)**: Time-domain simulations of SMIB under random disturbances. **(c)**: Samples in the classical feature space (green for stable samples and red for unstable samples). **(d)**: Samples embedded in the Hilbert space by a randomly-initialized HELD. **(e)**: Loss function evolution during QTSA training process and the final confusion matrix. **(f)**: Samples embedded in the Hilbert space by the well-trained HELD, where the stable and unstable samples are distinctly separated. **(g)**: Stable and unstable regions discovered by the well-trained HELD and its comparison with the physical model-based analytic stability boundary (i.e., black line). **(h)**: Contour plot of probability on measuring $|1\rangle$ from HELD. Either a high probability on $|1\rangle$ or a high probability on $|0\rangle$ (i.e.,low probability on $|1\rangle$) reflects a high fidelity of transient stability prediction. **(i)**: Stability boundaries discovered by QTSA under different fidelity levels.

(θ, ϕ) on the Bloch sphere[1] represents a single-qubit state $\cos\frac{\theta}{2}|0\rangle + e^{i\phi} sin(\theta/2)|1\rangle$. The data overlap between each pair of samples represents the fidelity between the corresponding quantum states.

Starting with a randomly-initialized HELD, Fig. 3(d) shows that the stable and unstable samples are mixed on the Bloch sphere and quantum states corresponding to stable and unstable samples are highly overlapped, meaning the untrained circuit cannot be used for TSA. Then, Fig. 3(e) shows the evolution of loss function during the QTSA training, where the classification accuracy exceeds 99% for both stable and unstable samples at the final stage. The Hilbert space observations in Fig. 3(f) demonstrate the efficacy of the trained HELD. It can be seen that the well-trained quantum circuit successfully embeds the stable (unstable) samples to the lower-(upper-) half Bloch sphere. As can be seen from the data overlap, the mutual fidelity between samples from the same class is almost 1, while that from different classes is close to 0. Both observations verify a successful QTSA being able to clearly separate the opposite classes through the VQC.

3) Stability Insights by QTSA: Fig. 3(g) shows that QTSA is able to accurately discover power system stability regions $\mathcal{A}(Z_s)$ (see (2)). As illustrated by the simulation results, there is a faithful match between the stable/unstable regions learned by QTSA (i.e., the green and red regions) and those obtained from model-based analytical solutions (i.e., the black line). Stability regions discovered by QTSA allow power system operators to identify the system stability under disturbances, i.e., the SMIB system will remain stable if its post-contingency state locates in the green zone, whereas it must collapse if the post-contingency state locates in the red zone.

Another interesting observation is that QTSA offers not only the stability classification results but also the fidelity of stability or instability. Fidelity measures the similarity of quantum states [2]. Denote the output state of HELD at the first

[1]The Bloch sphere geometrically represents a single-qubit quantum states on a unit three-dimensional sphere. A state $|\psi\rangle = \alpha_0|0\rangle + \alpha_1|1\rangle$ can always be rewritten as $|\psi\rangle = e^{i\gamma}\left(\cos\frac{\theta}{2}|0\rangle + e^{i\phi}\cos\frac{\theta}{2}|1\rangle\right)$, where γ, θ, ϕ are real numbers. Therefore, θ and ϕ, as the spherical co-ordinates, jointly define a point on the Bloch sphere for $|\psi\rangle$.

[2]For two pure quantum states $|\psi_1\rangle = \sum \alpha_{1i}|i\rangle$ and $|\psi_2\rangle = \sum \alpha_{2i}|i\rangle$, their fidelity is defined as $F(\psi_1, \psi_2) = |\langle\psi_1|\psi_2\rangle|^2 = (\sum \alpha_{1i}^* \alpha_{2i})^2$.

This article has been accepted for publication in a future issue of this journal, but has not been fully edited. Content may change prior to final publication. Citation information: DOI 10.1109/TPWRS.2022.3160384, IEEE Transactions on Power Systems

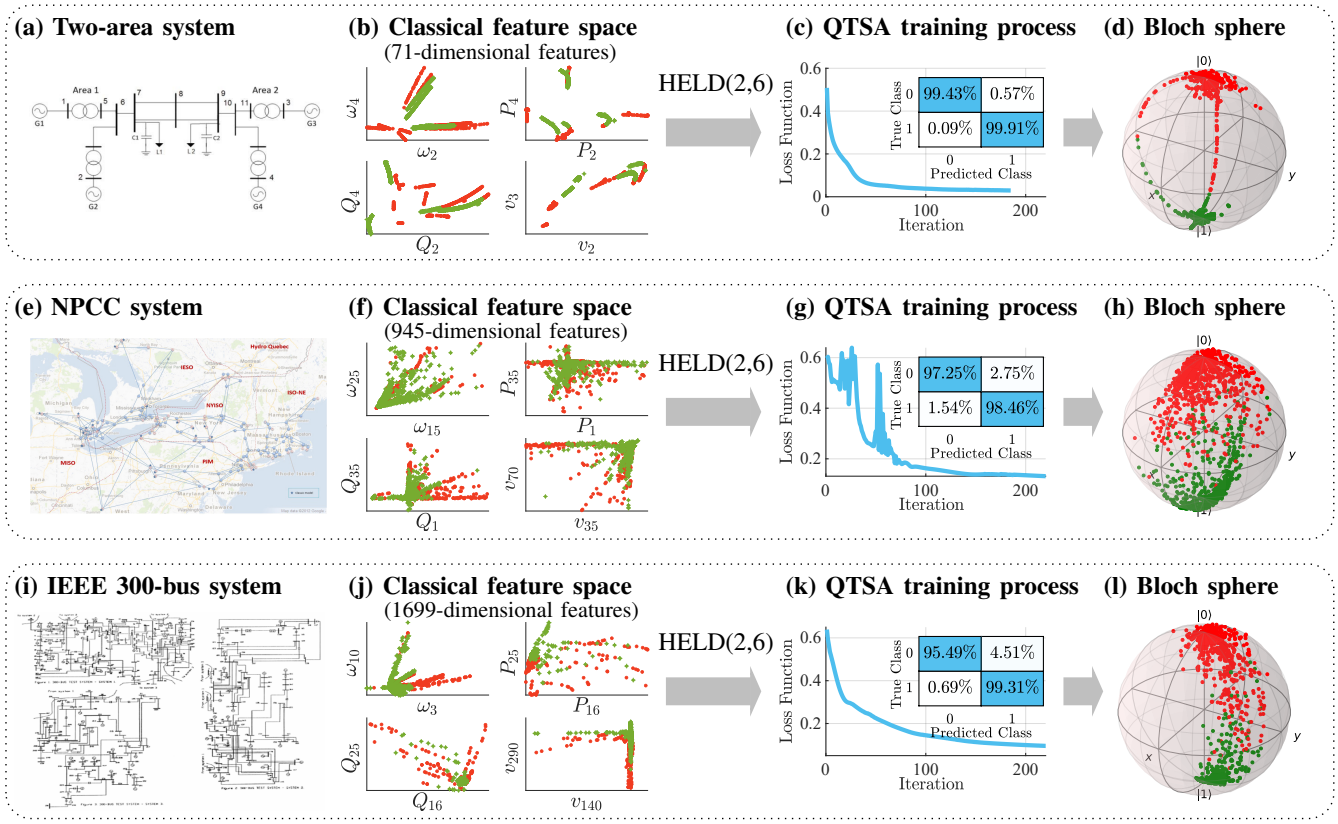

Fig. 4. **QTSA results for practical power systems**. Subplot (a-d), (e-h) and (i-l) respectively present QTSA results of the two-area system, the NPCC system and the IEEE 300-bus system. All the cases use HELD(2,6), where 2 qubits and 6 layers are employed. **(a)(e)(i)**: Power grid topology. **(b)(f)(j)**: Samples in the classical space (green for stable samples and red for unstable samples). In all the cases, stability features include power outputs, rotor angles and rotor speeds of generators, power flows through transmission lines, and bus voltage angles and amplitudes (ω, P, Q and v respectively denote the rotor speeds, active power generations, reactive power generations and bus voltage amplitudes). **(c)(g)(k)**: Loss function evolution during QTSA training process. **(d)(h)(l)**: State measurements of the trained HELD. Stable samples (green) and unstable samples (red) are embedded to different halves of the Block sphere.

qubit as $\psi = \alpha_0 |0\rangle + \alpha_1 |1\rangle$. The fidelities between ψ and stability (i.e., $|1\rangle$) and instability (i.e., $|0\rangle$) are respectively $F_1 = |\langle\psi|1\rangle|^2 = |\alpha_1|^2$ and $F_0 = |\langle\psi|0\rangle|^2 = |\alpha_0|^2$, which can be directly measured from the multi-shot executions of the quantum circuit.

As shown in Fig. 3(h), for a post-contingency state falling in the stable zone, the farther it deviates from the stability boundary, the system stability ($|1\rangle$) would be assured with a higher probability. Similarly, the system would collapse ($|0\rangle$) with a higher probability if its state lies in the deeper red zone. The operating points with probabilities near 0.5 indicate marginal cases, which are observed to be located near the stability boundary. The probabilities associated with system stability provide valuable new information for system operators and decision makers to make more suitable planning, operation and remedial action schemes. Either the risk-averse or risk-takers will then selectively use such information to optimize the social welfare and improve electricity resilience.

Further, QTSA is able to calculate stability regions at different risk levels. Fig. 3(i) exhibits the stability boundaries corresponding to different fidelity thresholds. Being less risk-tolerant leads to shrunken stability regions because higher fidelity levels are adopted.

4) Verification on Practical Power Systems: We further exhibit the versatility and efficacy of QTSA in the stability assessment of large power systems. Fig. 4 presents the QTSA results for the two-area system, the NPCC system and the IEEE 300-bus system. For each system, as shown in Fig. 4(b), (f) and (j), their high-dimensional features are irregularly distributed in the classical space and their stable/unstable samples are highly mixed. Once a trained HELD embeds the classical features into quantum states, it successfully arranges the stable and unstable samples onto the upper- and lower-halves of a Bloch sphere, rendering the challenging power system stability identification straightforward and effortless in the Hilbert space.

Table. I quantitatively evaluates the accuracy of QTSA. For the small- and medium-scale power system, QTSA achieves high accuracy on both the training set ($> 99\%$) and test set ($> 98\%$). Even for the large-scale systems such as the NPCC grid and IEEE 300-bus grid, QTSA exhibits satisfactory performance of 98% accuracy on the training set and 95% accuracy on the testing set. QTSA is further compared with two data-driven TSA methods based on classical machine learning, i.e., a support vector machine (SVM) with the radial basis function kernel, and a deep neural network (DNN) with a three-layer perceptron architecture implemented in Scikit-learn [39]. Both the F_1-scores and accuracy validate QTSA's competency and high performance in comparison with classical data-driven TSA approaches.

TABLE I. **Comparison of accuracy: QTSA vs. TSA based on classical machine learning methods**

		Training Set			Test Set		
		QML	SVM	DNN	QML	SVM	DNN
SMIB System	Accuracy	0.9906	0.9525	0.9913	0.9810	0.9510	0.9865
	Precision	0.9867	0.9672	0.9867	0.9726	0.9754	0.9855
	Recall	0.9911	0.9185	0.9926	0.9820	0.9050	0.9820
	F_1-Score	0.9889	0.9422	0.9897	0.9773	0.9389	0.9837
Two-Area System	Accuracy	0.9975	0.9931	0.9944	0.9860	0.9900	0.9850
	Precision	0.9972	0.9917	0.9917	0.9795	0.9866	0.9779
	Recall	0.9991	0.9981	1.0000	1.0000	0.9985	1.0000
	F_1-Score	0.9981	0.9949	0.9958	0.9896	0.9925	0.9888
NPCC System	Accuracy	0.9800	0.9550	0.9765	0.9530	0.9470	0.9560
	Precision	0.9831	0.9442	0.9822	0.9560	0.9455	0.9582
	Recall	0.9846	0.9854	0.9798	0.9722	0.9757	0.9757
	F_1-Score	0.9838	0.9644	0.9810	0.9640	0.9604	0.9669
IEEE 300-bus System	Accuracy	0.9800	0.9385	0.9645	0.963	0.9300	0.9460
	Precision	0.9768	0.9349	0.9573	0.9674	0.937	0.9397
	Recall	0.9931	0.9741	0.9901	0.9775	0.9595	0.9820
	F1-Score	0.9849	0.9541	0.9734	0.9724	0.9481	0.9604

[1] Accuracy $= \frac{TP+TN}{TP+TN+FP+FN}$; Precision $= \frac{TP}{TP+FP}$; Recall $= \frac{TP}{TP+FN}$; F_1-Score$= 2(\text{Precision}^{-1}+\text{Recall}^{-1})^{-1}$. Here, TP, TN, FP, FN respectively denote the number of true positive, true negative, false positive and false negative samples.

B. Comparison of Quantum Circuits

In this section, we demonstrate how different designs of quantum circuits impact the quantum TSA's performance. Three factors are taken into consideration: circuit depth (i.e., number of layers), circuit width (i.e., number of qubits) and circuit layer structure. In addition to classification accuracy and F_1-Score, another performance index $Tr(\sigma_0\sigma_1)$ is introduced for QTSA, where $\sigma_0 = \text{mean}_{i\in\mathcal{S}_0}(|\psi_i\rangle\langle\psi_i|)$ and $\sigma_1 = \text{mean}_{i\in\mathcal{S}_1}(|\psi_i\rangle\langle\psi_i|)$ respectively denote the mean density matrices of unstable/stable samples. A decrease in $Tr(\sigma_0\sigma_1)$ thus indicates an improved separation between the stable and unstable classes. Without loss of generality, the comparisonal studies are performed on the SMIB system.

1) Impact of Quantum Circuit Scale: Fig. 5 shows the impacts of scaling factors such as circuit's depths and widths. The following insights can be obtained:

- Initially, increasing the number of layers tends to cause improved accuracy and better separations between stable/unstable samples. The rationale behind this is an enhanced expressibility of the quantum circuit. Note that the performance of QTSA starts to saturate once the depth goes beyond a certain number (6 in this case).
- Increasing the number of qubits also leads to improved QTSA performance, whereas the expressibility saturation is again observed. A noteworthy observation is that QTSA manifests impressive expressibility even with a single qubit, where the classification accuracy still reaches 97.38%.
- Although more layers and qubits definitely boost the expressibility of HELD, an overscale quantum circuit is not recommended. Such a circuit would demand prohibitively expensive quantum resources due to the saturation phenomenon. It also aggravates the training burden of the variational quantum circuit accompanied with the increased parameters. Finally, a large-scale quantum circuit is prone to the noisy quantum environment, leading to a sharply declined TSA performance on real quantum devices (which will be further discussed in the next subsection).

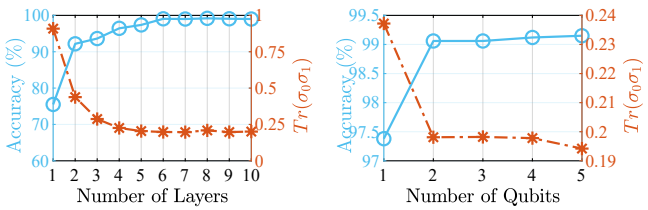

(a) Impact of circuit depth (b) Impact of circuit width

Fig. 5. **QTSA performances with different HELD circuit scales**. The architecture of HELD is depicted in Fig. 2. An improved separation between the stable and unstable classes is indicated by improved accuracy and decreased $Tr(\sigma_0\sigma_1)$.

2) Impact of Circuit Layer Structure: Fig. 6 compares the performance of HELD with those of three typical variational quantum circuit (VQC) structures, i.e., an Instantaneous Quantum Polynomial (IQP) circuit [24], the Quantum Approximate Optimization Algorithm (QAOA) inspired circuit [25], and a data reuploading circuit [30]. Our HELD circuit exhibits the best expressibility benefiting from its non-Gaussian feature encoding and entanglement layers.

Further, we quantitatively analyze the expressibility of HELD. Two expressibility indices are introduced: E_{Haar} describes a VQC's ability to express the Hilbert space [29], and E_{TSA} describes a VQC's ability to express the TSA classification.

$$E_{Haar} = D_{KL}(P_{VQC}(f,\boldsymbol{p})||P_{Haar}(f)) \tag{15}$$

$$E_{TSA} = D_{KL}(P_{VQC}(f_y,\boldsymbol{p}^*)||P_{TSA}(f_y)) \tag{16}$$

Both E_{Haar} and E_{TSA} are defined based on the Kullback-Leibler (KL) divergence $D_{KL}(P||Q) = \sum_i P(i)\ln\frac{P(i)}{Q(i)}$, which is widely used in machine learning to quantify the difference between an estimated distribution P and the ideal distribution Q. A smaller KL-divergence indicates a better expressibility. Specifically, E_{Haar} denotes the KL divergence between $P_{VQC}(f,\boldsymbol{p})$ (i.e., the distribution of fidelity f estimated from a VQC parameterized by $\boldsymbol{p}$) and the Haar distribution $P_{Haar}(f)$ (i.e., the probability distribution under the Haar random states) [29]. E_{TSA} denotes the KL divergence between $P_{VQC}(f_y,\boldsymbol{p}^*)$ (i.e., the distribution of the stability fidelity $f_y = |\langle 1|U(\boldsymbol{p}^*)|0\rangle\rangle|^2$ estimated by the optimized VQC) and $P_{TSA}(f_y)$ (i.e., the true distribution of stability fidelity obtained from the ground truth).

Fig. 7 and Fig. 8 present the simulation results. Fig. 7 shows that probability distributions estimated by those VQCs all match well with the Haar distribution and HELD exhibits slightly better performance. This observation indicates that each VQC can properly express the quantum states in the whole Hilbert space. Actually, as investigated in [29], a VQC with enough parameterized rotation gates and entanglements usually can represent the Hilbert space effectively. Nevertheless, simulation results in Fig. 8 show that those VQCs exhibit essentially different expressibility for TSA classifications. HELD achieves the best performance regarding E_{TSA}. In contrast, other types of VQCs lead to considerable KL divergence between the true stability distribution and the estimated stability distribution, which conforms with the fact that they mix plenty of stable and unstable samples. This

This article has been accepted for publication in a future issue of this journal, but has not been fully edited. Content may change prior to final publication. Citation information: DOI 10.1109/TPWRS.2022.3160384, IEEE Transactions on Power Systems

Circuit Layer Structure	Evaluation Indices		Stability Region	Bloch Sphere
Our HELD(2,6) circuit 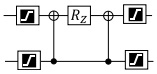	Accuracy	0.9906	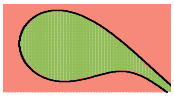	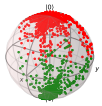
	F_1-Score	0.9889		
	$Tr(\sigma_0\sigma_1)$	0.1981		
IQP circuit [24] 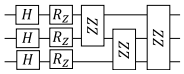	Accuracy	0.8688		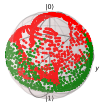
	F_1-Score	0.8241		
	$Tr(\sigma_0\sigma_1)$	0.5636		
QAOA circuit [25] 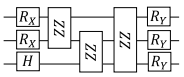	Accuracy	0.8994	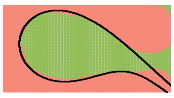	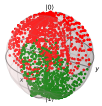
	F_1-Score	0.8851		
	$Tr(\sigma_0\sigma_1)$	0.4685		
Data reuploading [30] 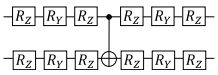	Accuracy	0.9206	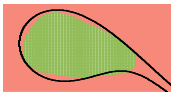	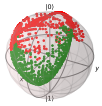
	F_1-Score	0.8993		
	$Tr(\sigma_0\sigma_1)$	0.4379		

Fig. 6. **Quantum TSA performances with different quantum circuit designs**. Our HELD circuit employs 2 qubits and 6 layers. The IQP and QAOA circuits both employ 3 qubits and 10 layers. The data reuploading circuit employs 2 qubit and 10 layers. Three indices are employed to evaluate the transient stability prediction capability of quantum circuits: classification accuracy, F_1-Score and $Tr(\sigma_0\sigma_1)$. An improved separation between the stable and unstable classes is indicated by improved accuracy, increased F_1-Score and decreased $Tr(\sigma_0\sigma_1)$.

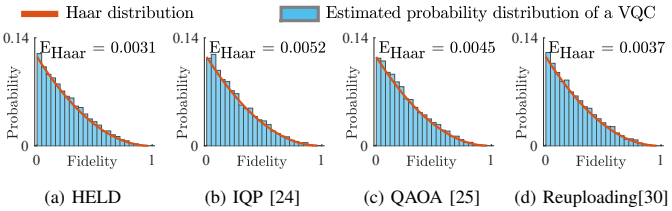

(a) HELD (b) IQP [24] (c) QAOA [25] (d) Reuploading[30]

Fig. 7. Expressibility of different VQCs for exploring the Hilbert space

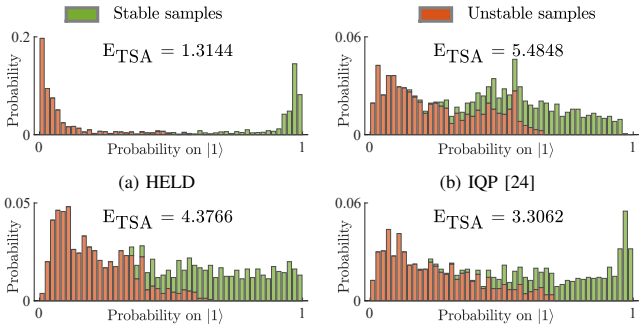

(a) HELD (b) IQP [24] (c) QAOA [25] (d) Reuploading [30]

Fig. 8. Expressibility of different VQCs for TSA classifications

observation shows that HELD not only explores the Hilbert space effectively but also well expresses the stable and unstable samples.

C. Validity of QTSA on Real, Noisy Quantum Environment

Today's quantum devices are limited by gate errors and qubit connectivity, which hinders the implementation of deep quantum circuits. As an ultimate test of the practicality of QTSA, we now implement it on a real quantum computer and systematically verify it under noisy quantum computing environments.

1) Verification on the Real IBM Quantum Computers: In this subsection, we run QTSA on real IBM Quantum device. QTSA of the SMIB system, 2-area system and NPCC system is tested on *ibmq_boelingen* which is a 20-qubit superconducting quantum computer (QC). QTSA of the IEEE 300-bus system is tested on a 7-qubit QC *ibm_lagos*. The number of shots is set as 1024. Fig. 9 presents the configuration of *ibmq_boelingen* as well as its error map. The average error rates of the single-qubit Hadamard gate and the double-qubit CNOT gate are respectively 0.038% and 1.308%.

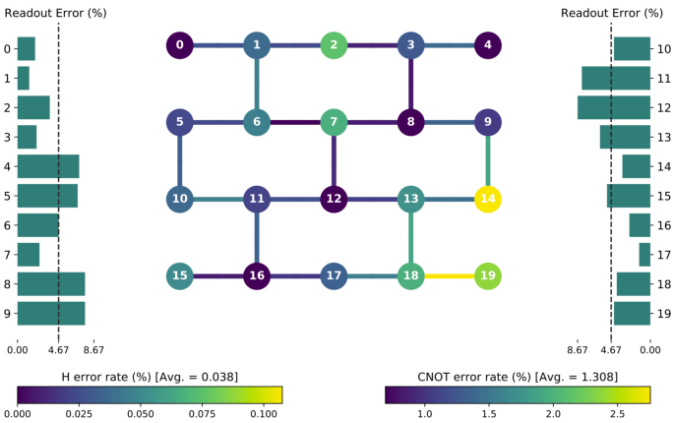

Fig. 9. **Configuration and error map of the ibmq_boelingen 20-qubit quantum computer.** Figure courtesy of IBM TJ Watson Research Center [40]

Table. II presents QTSA's accuracy obtained from real IBM quantum computers, where the stability identification results are again obtained by HELD(2,6). Compared with those results on the noise-free IBM Quantum simulator *ibmq_qasm_simulator*, a surprising finding is that a noisy real quantum computing environment has little effect on the performance of QTSA and the overall classification is still of high quality. Even in the most challenging case of the IEEE 300-bus system, only a 0.5% decrease in the accuracy is reported, and the QTSA results remain compelling as compared with those from classical machine learning algorithms (see Table. I). This experiment exhibits the effectiveness of QTSA on the near-term quantum devices and verifies the inherent resilience of QTSA against noisy quantum computing environments.

Fig. 10(a) further investigates the rationale behind the resilience of QTSA. Accordingly, there are four types of results:

This article has been accepted for publication in a future issue of this journal, but has not been fully edited. Content may change prior to final publication. Citation information: DOI 10.1109/TPWRS.2022.3160384, IEEE Transactions on Power Systems

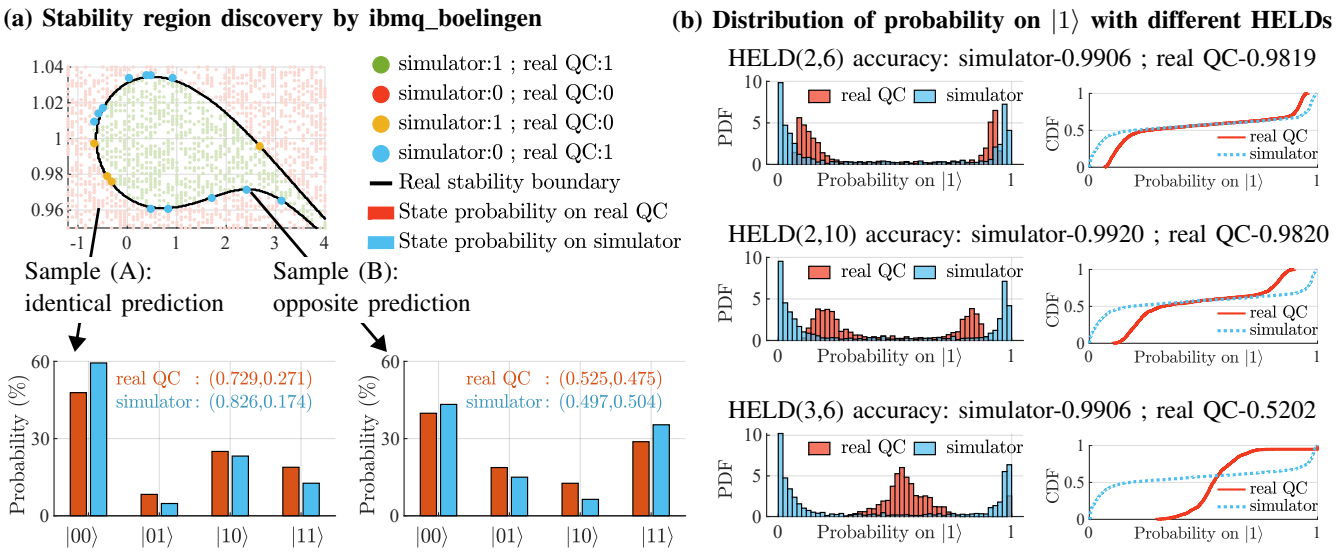

Fig. 10. **Implementation of QTSA on the noisy IBM Quantum computer (*ibmq_boelingen*). (a)**: Stability predictions obtained on the simulator *ibmq_qasm_simulator* and the real noisy QC *ibmq_boelingen*. Two typical samples exemplify the quantum state probability measured from HELD. Sample (A) illustrates an identical prediction on both devices, which represents the most cases (green and red dots), whereas sample (B) illustrates an opposite prediction, which is observed mainly around the stability boundary. **(b)**: Probability distribution function (PDF) and cumulative distribution function (CDF) of the probability of measuring $|1\rangle$ from different-scaled HELD circuits.

TABLE II. **Comparison of QTSA accuracy: noisy real quantum devices vs. noise-free simulator *ibmq_qasm_simulator***

		Training Set		Test Set	
		Real QC	Simulator	Real QC	Simulator
SMIB System	Accuracy	0.9819	0.9906	0.9770	0.9810
	Precision	0.9708	0.9867	0.9679	0.9726
	Recall	0.9867	0.9911	0.9772	0.9820
	F_1-Score	0.9787	0.9889	0.9725	0.9773
Two-Area System	Accuracy	0.9907	0.9975	0.9910	0.9930
	Precision	0.9882	0.9972	0.9866	0.9896
	Recall	0.9980	0.9991	1.0000	1.0000
	F_1-Score	0.9931	0.9981	0.9933	0.9948
NPCC System	Accuracy	0.9710	0.9800	0.9450	0.9540
	Precision	0.9727	0.9831	0.9414	0.9527
	Recall	0.9806	0.9846	0.9772	0.9787
	F_1-Score	0.9767	0.9838	0.9590	0.9655
IEEE 300-bus System	Accuracy	0.9780	0.9800	0.9590	0.9630
	Precision	0.9746	0.9768	0.9658	0.9674
	Recall	0.9924	0.9931	0.9730	0.9775
	F1-Score	0.9834	0.9849	0.9694	0.9724

green dots (samples predicted as stable on both the simulator *ibmq_qasm_simulator* and the real QC *ibmq_boelingen*); red dots (samples predicted as unstable on both devices); yellow dots (samples predicted as stable on the simulator but unstable on the real QC); blue dots (samples predicted as unstable on the simulator but stable on the real QC). It can be seen that samples of inconsistent prediction from *ibmq_boelingen* and *ibmq_qasm_simulator* (i.e., the blue and yellow dots) are mostly distributed around the stability boundary. Further, Fig. 10(a) exemplifies the quantum state probability measured from HELD by two typical samples. Sample (A) illustrates an identical prediction on both devices, which represents the most cases (green and red dots), whereas sample (B) illustrates an opposite prediction, which is observed mainly around the stability boundary. The measurement probability distribution of samples (A) and (B) shows that the measurement probabilities from *ibmq_boelingen* and *ibmq_qasm_simulator* do not differ much. This indicates HELD(2,6) is only slightly perturbed by the noisy quantum device. Therefore, only for the low-fidelity areas where the quantum circuit output already has a similar probability on both $|0\rangle$ and $|1\rangle$, a slight perturbation from the noisy environment would possibly produce an opposite classification result, as exemplified by sample (B). According to our previous study in Fig. 3(h), those samples locate in a narrow area around the stability boundary, which are actually of low stability margin, and thus their stability by their very nature is uncertain. Whereas, for the high-fidelity areas as exemplified by sample (A), the quantum circuit output in the noisy device does not change the final QTSA prediction. Therefore, QTSA generates reliable results for most samples even on noisy QCs.

Even though HELD(2,6) maintains high accuracy, a larger scale HELD circuit may fail to produce similar results. Fig. 10(b) illustrates the performance of HELD of different scales on noisy QCs, where HELD(2,6) as the default case, HELD(2,10) with 10 layers and HELD(3,6) with an additional qubit are compared.

- On the first qubit (i.e., the output qubit), we measure its probability on the basis quantum state $|1\rangle$ based on 1024 shots. Denote the probability on $|1\rangle$ as $|\alpha_1|^2$. By gathering $|\alpha_{1,i}|^2$ for each sample i $(\forall i = 1, \ldots, n)$, the probability density function of $|\alpha_1|^2$ can be estimated. The x-axis and y-axis of Fig. 10(b) correspondingly refer to $|\alpha_1|^2$ and the PDF/CDF of $|\alpha_1|^2$. To best classify the stable and unstable samples, $|\alpha_1|^2$ is expected to be concentrated around 0 and 1 (i.e., high fidelity for instability/stability).
- On the noise-free *ibmq_qasm_simulator*, all circuits achieve high accuracy over 99% with a notable feature that quantum measurements mainly accumulate around 0 and 1. This indicates that most samples are predicted at high confidences, which is coincident with Fig.3(h), i.e., only the narrow areas around the stability boundary are of low fidelity.
- For HELD(2,6) running on the noisy *ibmq_boelingen*, the

This article has been accepted for publication in a future issue of this journal, but has not been fully edited. Content may change prior to final publication. Citation information: DOI 10.1109/TPWRS.2022.3160384, IEEE Transactions on Power Systems

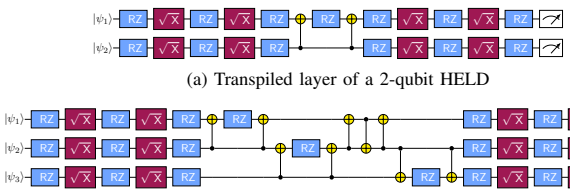

(a) Transpiled layer of a 2-qubit HELD

(b) Transpiled layer of a 3-qubit HELD

Fig. 11. Transpiled HELD circuit on the real QC *ibm_lagos*

peaks of the probability distribution slightly shift towards the center compared with that from the simulator, indicating a slightly decreased prediction fidelity.

- For HELD(2,10), although its accuracy on the noisy QC remains comparable to that of HELD(2,6), the shift of probability distribution peaks is more obvious, reflecting a further decreased fidelity on the noisy prediction.
- For HELD(3,6) involving more qubits, more CNOT gates and deeper circuit depth, the accuracy on the real QC deteriorates down to 52.02%, making the evaluation on the noise-free simulator meaningless. The probability distribution histogram shows most of the measurements center around 0.5, indicating that output states from QTSA are nearly random due to the noisy environment and quantum decoherence.
- The degraded performance of HELD(3,6) is induced by the increased number of CNOT gates. On the one hand, the theoretical design of HELD (see Fig. 2) requires more CNOT gates in each layer when more qubits are employed. On the other hand, in the real-machine implementation, if a CNOT gate is required between two disconnected qubits, the quantum circuit will be transpiled using SWAP, which also increases the number of CNOT gates. Fig. 11 shows the transplied HELD circuit on the real QC *ibm_lagos*. [3] It can be observed that for the 2-qubit case, the arrangement of CNOT gates executed on the real QC conforms with the design in Fig. 2. Nevertheless, for the 3-qubit case, the HELD circuit is transplied because qubit 3 is not connected to qubit 1, and therefore, three additional CNOT gates are involved. Since two-qubit gates always introduce more significant errors than single-qubit gates, more CNOT gates lead to reduced noise resilience.
- Consequently, a high quality QTSA need to possess both high accuracy and high fidelity. This is important to ensure a high tolerance against noises.

Additionally, Table III presents the runtime of the quantum-based TSA on the real QC *ibm_lagos*. The runtime of each job in IBM Qiskit mainly comprises the time consumption for transpilation, validation, and execution.

2) Impact of Various Noise Levels: Since different quantum devices may have different noise features, it is necessary to systematically examine the QTSA's performance under various noisy environments. We adjust the noise levels through a noise module provisioned by IBM and the noise settings are modified from the *ibmq_boelingen*'s real noise data. As Fig. 12 shows, excessive gate error and decohenrece time certainly lead to the collapse of the quantum circuit. Nevertheless, high TSA accuracy can still be obtained with gate errors smaller than 2% or the thermal relaxation time larger than 10μs, which can be easily satisfied by today's quantum hardware. The QTSA's excellent performance is therefore universal.

3) Remarks: (a) With HELD, quantum computers with limited qubit resources can still handle high-dimensional TSA problems and achieve satisfactory accuracy. The reason is because HELD employs TSA features as rotation parameters of the controllable quantum gates (see the parameterized rotation angles θ in (4), (5) and (6)) rather than encoding them into quantum states. The feature dimension that QTSA can handle thus is independent of the number of qubits. (b) Due to quantum noises, it is more challenging to implement a quantum circuit on near-term quantum computers than on quantum simulators or noise-free quantum computers in a distant future. This necessitates the design of a low-depth quantum circuit. (c) The unique potentials of QTSA over classical ML-based TSA are as follows. First, the execution of the quantum circuit refers to computations in the Hilbert space, as presented in (4)-(6), which inherits the exponential quantum speedup in tensor products. Second, QTSA reports comparable accuracy against classical DNN while saving more

[3]The IBM quantum computer *ibm_lagos* only has 5 basis gates, i.e., CX (the controlled-X gate), ID (the identity gate), RZ (the single-qubit rotation about the Z axis), X (the Pauli-X gate) and SX (the sqrt-X gate). Therefore, when executed on *ibm_lagos*, the RX and RY gates designed in Fig. 2 are transpiled to basis gates (i.e., RZ gates, CX gates and SX gates) in Fig. 11.

TABLE III. **Runtime of QTSA on *ibm_lagos* (unit: s)**

HELD Scale	Transpilation	Validation	Execution	Sum
(2,2)	0.919	1.173	4.931	7.023
(2,4)	0.750	1.221	4.892	6.863
(2,6)	0.842	1.136	5.022	7.000
(2,8)	0.766	0.999	4.988	6.753
(3,2)	0.900	1.579	5.296	7.775
(3,4)	0.625	1.177	5.078	6.880
(3,6)	0.832	0.845	5.179	6.856
(3,8)	0.828	1.080	5.174	7.082

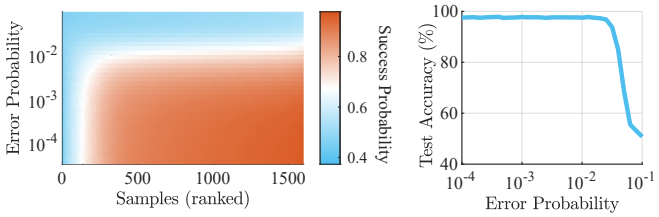

(a) QTSA performance over a range of gate errors

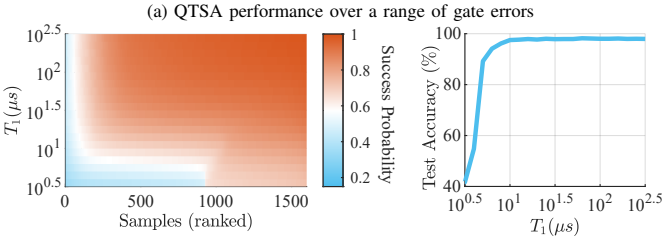

(b) QTSA performance over a range of thermal relaxation time

Fig. 12. **Impact of noisy quantum environment on QTSA performance**. **(a)**: Left subplot shows QTSA's success probabilities of all samples (sorted from the sample of the lowest success probability to that of the highest) over a range of gate errors. Right subplot shows QTSA's overall accuracy on the test set over a range of gate errors. **(b)**: QTSA's success probabilities of all sample as well as the overall accuracy over a range of thermal relaxation time T_1 (i.e., the time it takes for a qubit to decay from the excited state to the ground state).

than 70% parameters, which conforms to the observations in existing studies that QML can be more expressive [41].

IV. Conclusion

This paper unlocks the potential of quantum machine learning in power system data-driven analytics. The key innovation is to develop a HELD circuit-centric transient stability assessment to enable an efficient transient stability analysis for resilient and secured decision-making of real-world power systems. The new quantum transient stability analysis algorithm achieves outstanding performances both on a quantum simulator and real IBM quantum devices (*ibmq_boeblingen*, a 20-qubit machine, and *ibm_lagos*, a 7-qubit machine). Therefore, it has the penitential to resolve the TSA challenge in this noisy-intermediate-scale quantum (NISQ) era.

Acknowledgement

We would like to acknowledge the Brookhaven National Laboratory operated IBM-Q Hub. We thank Prof. Tzu-Chieh Wei (C.N. Yang Institute for Theoretical Physics and Department of Physics and Astronomy, Stony Brook University) for the valuable suggestions on the manuscript.

Appendix A
Test System Parameters and Training Settings

This appendix provides the test system parameters and dataset settings.

SMIB system: The dynamical model of the SMIB system is detailed as follows [5]:

$$\begin{aligned} \dot{\delta} &= \omega_0(\omega - 1) \\ \dot{\omega} &= \frac{1}{T_j}(P_m - P_e - D(\omega - 1)) \end{aligned} \tag{17}$$

Here, δ denotes the power angle (unit:rad) of the generator; ω denotes the rotor speed (unit: p.u.) of the generator; T_j and D respectively denote the inertia constant and damping coefficient; P_m is the mechanical power; $P_e = E'U_0 \sin\delta / x_0$ is the electrical power where E', U_0 and x_0 respectively denote the generator voltage, the infinite bus voltage and the equivalent impedance. Parameters of the SMIB system are: $\omega_0 = 120\pi$rad/s, $T_j = 6$s, $D = 5$p.u., $P_m = 1.2$p.u., $E' = 1.05$p.u., $U_0 = 1$p.u., $x_0 = 0.5$p.u..

Two-area system and NPCC system: All the parameters of the systems are from the Power System Toolbox (PST) [38]. The voltage-behind-transient-reactance model is adopted for all the synchronous generators.

IEEE 300-bus system: Parameters of the network and the operating point are from Matpower [42]. Dynamical models and parameters of the generators are from PST [38]. The classical generator model is adopted with a typical parameter setting (e.g., the d-axis synchronous reactance is 0.081 p.u. and the inertia constant is 30.3s).

Dataset settings: For the SMIB system, we perform time-domain simulations with randomly-generated initial states.

For other test systems, we perform time-domain simulations under three-phase short circuit faults. The initial operating points are identical to those from PST/Matpower. The fault location is randomly selected at different transmission lines. The fault clearing time is randomly set between 0.1s-0.35s for the 2-area system, 0.1s-0.55s for the NPCC system, and 0.1s-0.4s for the IEEE 300-bus system.

The obtained data are randomly divided into the training and testing sets.

References

[1] M. Singh, "'California and Texas are warnings': blackouts show US deeply unprepared for the climate crisis," *The Guardian*, Feb. 19, 2021.
[2] California ISO, California Public Utilities Commission, and California Energy Commission, "Root cause analysis: Mid-August 2020 extreme heat wave," tech. rep., Jan. 13, 2021.
[3] Department of Energy, "Transforming the nation's electricity system: The second installment of the quadrennial energy review," tech. rep., Washington DC, 2017.
[4] B. A. Carreras, D. E. Newman, and I. Dobson, "North American blackout time series statistics and implications for blackout risk," *IEEE Transactions on Power Systems*, vol. 31, no. 6, pp. 4406–4414, 2016.
[5] P. Kundur, *Power System Stability and Control*. McGraw-Hill, 1994.
[6] J. James, D. J. Hill, A. Y. Lam, J. Gu, and V. O. Li, "Intelligent time-adaptive transient stability assessment system," *IEEE Transactions on Power Systems*, vol. 33, no. 1, pp. 1049–1058, 2017.
[7] Y. Xu, Z. Y. Dong, J. H. Zhao, P. Zhang, and K. P. Wong, "A reliable intelligent system for real-time dynamic security assessment of power systems," *IEEE Transactions on Power Systems*, vol. 27, no. 3, pp. 1253–1263, 2012.
[8] M. Benidris, J. Mitra, and C. Singh, "Integrated evaluation of reliability and stability of power systems," *IEEE Transactions on Power Systems*, vol. 32, no. 5, pp. 4131–4139, 2017.
[9] A. Iravani and F. De Leon, "Real-time transient stability assessment using dynamic equivalents and nonlinear observers," *IEEE Transactions on Power Systems*, 2020.
[10] H.-D. Chiang and L. F. Alberto, *Stability Regions of Nonlinear Dynamical Systems: Theory, Estimation, and Applications*. Cambridge University Press, 2015.
[11] M. Kabalan, P. Singh, and D. Niebur, "Large signal lyapunov-based stability studies in microgrids: A review," *IEEE Transactions on Smart Grid*, vol. 8, no. 5, pp. 2287–2295, 2016.
[12] H.-D. Chiang, "Study of the existence of energy functions for power systems with losses," *IEEE Transactions on Circuits and Systems*, vol. 36, no. 11, pp. 1423–1429, 1989.
[13] L. Zheng, W. Hu, Y. Zhou, Y. Min, X. Xu, C. Wang, and R. Yu, "Deep belief network based nonlinear representation learning for transient stability assessment," in *2017 IEEE Power & Energy Society General Meeting*, pp. 1–5, IEEE, 2017.
[14] A. G. Phadke and J. S. Thorp, *Synchronized Phasor Measurements And Their Applications*. Springer, 2008.
[15] A. W. Harrow and A. Montanaro, "Quantum computational supremacy," *Nature*, vol. 549, no. 7671, pp. 203–209, 2017.
[16] F. Arute, K. Arya, R. Babbush, D. Bacon, J. C. Bardin, R. Barends, R. Biswas, S. Boixo, F. G. Brandao, D. A. Buell, *et al.*, "Quantum supremacy using a programmable superconducting processor," *Nature*, vol. 574, no. 7779, pp. 505–510, 2019.
[17] J. Biamonte, P. Wittek, N. Pancotti, P. Rebentrost, N. Wiebe, and S. Lloyd, "Quantum machine learning," *Nature*, vol. 549, no. 7671, pp. 195–202, 2017.
[18] M. A. Nielsen and I. L. Chuang, *Quantum Computation and Quantum Information: 10th Anniversary Edition*. Cambridge University Press, 2010.
[19] S. Lloyd, M. Mohseni, and P. Rebentrost, "Quantum algorithms for supervised and unsupervised machine learning," *arXiv preprint arXiv:1307.0411*, 2013.
[20] P. Wittek, *Quantum Machine Learning: What Quantum Computing Means To Data Mining*. Academic Press, 2014.
[21] M. Schuld, *Supervised Learning With Quantum Computers*. Springer, 2018.
[22] S. Lloyd, M. Mohseni, and P. Rebentrost, "Quantum principal component analysis," *Nature Physics*, vol. 10, no. 9, pp. 631–633, 2014.
[23] K. Beer, D. Bondarenko, T. Farrelly, T. J. Osborne, R. Salzmann, D. Scheiermann, and R. Wolf, "Training deep quantum neural networks," *Nature Communications*, vol. 11, no. 1, pp. 1–6, 2020.
[24] V. Havlíček, A. D. Córcoles, K. Temme, A. W. Harrow, A. Kandala, J. M. Chow, and J. M. Gambetta, "Supervised learning with quantum-enhanced feature spaces," *Nature*, vol. 567, no. 7747, pp. 209–212, 2019.

[25] S. Lloyd, M. Schuld, A. Ijaz, J. Izaac, and N. Killoran, "Quantum embeddings for machine learning," *arXiv preprint arXiv:2001.03622*, 2020.
[26] S. Boixo, S. V. Isakov, V. N. Smelyanskiy, R. Babbush, N. Ding, Z. Jiang, M. J. Bremner, J. M. Martinis, and H. Neven, "Characterizing quantum supremacy in near-term devices," *Nature Physics*, vol. 14, no. 6, pp. 595–600, 2018.
[27] C. Bravo-Prieto, R. LaRose, M. Cerezo, Y. Subasi, L. Cincio, and P. Coles, "Variational quantum linear solver: A hybrid algorithm for linear systems," *Bulletin of the American Physical Society*, vol. 65, 2020.
[28] A. Kandala, A. Mezzacapo, K. Temme, M. Takita, M. Brink, J. M. Chow, and J. M. Gambetta, "Hardware-efficient variational quantum eigensolver for small molecules and quantum magnets," *Nature*, vol. 549, no. 7671, pp. 242–246, 2017.
[29] S. Sim, P. D. Johnson, and A. Aspuru-Guzik, "Expressibility and entangling capability of parameterized quantum circuits for hybrid quantum-classical algorithms," *Advanced Quantum Technologies*, vol. 2, no. 12, p. 1900070, 2019.
[30] A. Pérez-Salinas, A. Cervera-Lierta, E. Gil-Fuster, and J. I. Latorre, "Data re-uploading for a universal quantum classifier," *Quantum*, vol. 4, p. 226, 2020.
[31] J. R. McClean, S. Boixo, V. N. Smelyanskiy, R. Babbush, and H. Neven, "Barren plateaus in quantum neural network training landscapes," *Nature Communications*, vol. 9, no. 1, pp. 1–6, 2018.
[32] K. Mitarai, M. Negoro, M. Kitagawa, and K. Fujii, "Quantum circuit learning," *Physical Review A*, vol. 98, no. 3, p. 032309, 2018.
[33] J. Stokes, J. Izaac, N. Killoran, and G. Carleo, "Quantum natural gradient," *Quantum*, vol. 4, p. 269, 2020.
[34] N. Yamamoto, "On the natural gradient for variational quantum eigensolver," *arXiv preprint arXiv:1909.05074*, 2019.
[35] D. P. Kingma and J. Ba, "Adam: A method for stochastic optimization," *arXiv preprint arXiv:1412.6980*, 2014.
[36] H. Abraham, AduOffei, and R. Agarwal, "Qiskit: An open-source framework for quantum computing," 2019.
[37] V. Bergholm, J. Izaac, M. Schuld, C. Gogolin, M. S. Alam, S. Ahmed, J. M. Arrazola, C. Blank, A. Delgado, S. Jahangiri, *et al.*, "Pennylane: Automatic differentiation of hybrid quantum-classical computations," *arXiv preprint arXiv:1811.04968*, 2018.
[38] J. H. Chow and K. W. Cheung, "A toolbox for power system dynamics and control engineering education and research," *IEEE transactions on Power Systems*, vol. 7, no. 4, pp. 1559–1564, 1992.
[39] F. Pedregosa, G. Varoquaux, A. Gramfort, V. Michel, B. Thirion, O. Grisel, M. Blondel, P. Prettenhofer, R. Weiss, V. Dubourg, J. Vanderplas, A. Passos, D. Cournapeau, M. Brucher, M. Perrot, and E. Duchesnay, "Scikit-learn: Machine learning in Python," *Journal of Machine Learning Research*, vol. 12, pp. 2825–2830, 2011.
[40] A. D. Córcoles, A. Kandala, A. Javadi-Abhari, D. T. McClure, A. W. Cross, K. Temme, P. D. Nation, M. Steffen, and J. M. Gambetta, "Challenges and opportunities of near-term quantum computing systems," *arXiv preprint arXiv:1910.02894*, 2019.
[41] S. Y.-C. Chen, T.-C. Wei, C. Zhang, H. Yu, and S. Yoo, "Hybrid quantum-classical graph convolutional network," *arXiv preprint arXiv:2101.06189*, 2021.
[42] R. D. Zimmerman, C. E. Murillo-Sánchez, and R. J. Thomas, "Matpower: Steady-state operations, planning, and analysis tools for power systems research and education," *IEEE Transactions on power systems*, vol. 26, no. 1, pp. 12–19, 2010.

Yifan Zhou (S'15−M'20) received the B.S. degree in electrical engineering from Tsinghua University, Beijing, China, in 2014, and the Ph.D. degree in electrical engineering from Tsinghua University, Beijing, China, in 2019. She is currently a Postdoctoral Researcher with Stony Brook University, Stony Brook, NY, USA. Her research interests include microgrid stability and control, formal methods and reachability analysis, and quantum computing.

Peng Zhang (Senior Member, IEEE) received the Ph.D. degree in electrical engineering from the University of British Columbia, Vancouver, BC, Canada, in 2009. He is a Full Professor of Electrical and Computer Engineering, and a SUNY Empire Innovation Professor at Stony Brook University, New York. He has a joint appointment at Brookhaven National Laboratory as a Staff Scientist. Previously, he was a Centennial Associate Professor and a Francis L. Castleman Associate Professor at the University of Connecticut, Storrs, CT, USA. He was a System Planning Engineer at BC Hydro and Power Authority, Canada, during 2006-2010. His research interests include AI-enabled smart grids, quantum-engineered power grids, networked microgrids, power system stability and control, cybersecurity, and formal methods and reachability analysis.
Dr. Zhang is an individual member of CIGRÉ. He is an Editor for the IEEE Transactions on Power Systems, the IEEE Power and Energy Society Letters, and the IEEE Journal of Oceanic Engineering.